Journal of Non-Crystalline Solids 358 (2012) 1778–1782

Contents lists available at SciVerse ScienceDirect

Journal of Non-Crystalline Solids

journal homepage: www.elsevier.com/ locate/ jnoncrysol

Effect of germanium on the microstructure and the magnetic properties of Fe–B–Si amorphous alloys

D.C. Estévez *, I. Betancourt

Departamento de Materiales Metalicos y Ceramicos, Instituto de Investigaciones en Materiales, Universidad Nacional Autónoma de México, México D.F. 04510, Mexico

ARTICLE INFO

Article history:
Received 13 March 2012
Received in revised form 8 May 2012
Available online 4 June 2012

Keywords:
Soft magnetic properties;
Crystallization;
Ferromagnetic resonance

ABSTRACT

In this work, we present a systematic study on the crystallization kinetics and the magnetic properties of melt-spun $Fe_{80}B_{10}Si_{10-x}Ge_x$ ($x = 0.0 - 10.0$) amorphous alloys. The activation energy for crystallization, determined by differential scanning calorimetry, displayed a strong dependence on the Ge content, reflecting a deleterious effect on the alloys' thermal stability and their glass forming ability with increasing Ge concentration. On the other hand, the alloys exhibited excellent soft magnetic properties, i.e., high saturation magnetization values (around 1.60 T), alongside Curie temperatures of up to 600 K. Complementary, for increasing Ge substitution, the ferromagnetic resonance spectra showed a microstructural evolution comprising at least two different magnetic phases corresponding to a majority amorphous matrix and to Fe(Si, Ge) nanocrystallites for $x \geq 7.5$.

1. Introduction

Since the first amorphous alloy synthesized in the Au–Si system by rapid solidification [1], a large variety of metallic glasses have been developed during the subsequent four decades [2–9]. Among these materials, $Fe_{1-x}B_x$-based glassy alloys (with $15<x<30$) have been used in a wide range of applications as magnetic materials due to their excellent combination of soft magnetic properties, including high values of saturation magnetization, magnetic permeability and Curie temperature, together with very low power losses [4]. In fact, their current use in power electronic devices render them as an important group of engineering amorphous alloys [10]. In order to tailor the magnetic performance of these materials, alloying with transition metals (Co, Ni, Zr, Nb, Hf) and metalloids or non-metals atoms (Si, Ge or C, P) have proved to be useful, since a strong dependence of main intrinsic magnetic properties (namely, saturation magnetization and Curie temperature) with such alloying elements have been described with profusion [11–18]. In spite of the numerous reports regarding the impact of chemical composition variations on the physical properties of FeB-based amorphous alloys [19–26] and some other reports including the influence of Ge in another alloy systems [27–32], comparatively not one study can be found in the literature concerning the influence of the progressive addition of Ge in FeBSi alloys on their microstructure and magnetic properties. In this work, a systematic replacement of Si by Ge in the alloy system $Fe_{80}B_{10}Si_{10-x}Ge_x$ ($x = 0.0 - 10.0$ at.%) has been studied in order to determine the influence of such additions on their microstructure and magnetic properties.

2. Experimental techniques

Master ingots of 5.0 g were prepared from high purity elements Fe (99.99 wt.%), B (99.96 wt.%), Ge (99.9 wt.%), Si (99.9 wt.%) in an Ar arc-melting unit and were remelted four times to ensure chemical homogeneity, with little changes (below 1 mass%) of their weight after remelting. Metallic ribbons (20–30 μm thickness and 1.8 mm width) for each composition of the alloy series $Fe_{80}B_{10}Si_{10-x}Ge_x$ ($x = 0.0$, 2.5, 5.0, 5.0, 10.0 at.%) were produced by means of melt spinning technique into a sealed chamber under He atmosphere at a roll speed of 40 m/s. The microstructure of the as-cast alloys was determined by means of X-ray diffraction analysis (XRD) in a Siemens D5000 diffractometer with Co–K_α radiation and step size of 0.020° at 40 kV and 20 mA and by Transmission Electron Microscopy (TEM) in a Jeol 1200EX equipment operating at 120 kV. The crystallization kinetics was characterized by continuous heating in a differential scanning calorimeter (TA Instruments SDT Q600), by using variable heating rates between 5 and 25 K/min. As the reference plate the same empty aluminum capsule was used. On the other hand, room temperature magnetic measurements were carried out on as-quenched samples using Vibrating Sample Magnetometry (VSM) in a LDJ 9600 apparatus with a maximum applied field of 1360 kA/m, for which the uncertainty was estimated from the standard deviation after 10 repetitions. The equipment was calibrated using a high purity 2 mm nickel sphere of known mass and magnetic moment. Complementary, Curie temperature was determined using magnetic thermogravimetric analysis (MTGA) in a TA instruments 2950 thermobalance with a heating rate of 10 K/min, coupled with a permanent magnet. Ferromagnetic resonance (FMR) measurements were made by means of a Jeol JESRES3X spectrometer operating at 9.4 GHz (X-band) using horizontal-parallel orientation, i.e. the H_{dc} field is applied parallel the longitudinal ribbon axis and

* Corresponding author. Tel.: +52 44 5622 4642; fax: +52 44 5616 0754.
E-mail address: estevd@gmail.com (D.C. Estévez).

0022-3093/$ – see front matter © 2012 Elsevier B.V. All rights reserved.
doi:10.1016/j.jnoncrysol.2012.05.020

perpendicular to the H_{ac} field. Random errors are minimized due to the high precision (±1%) for both, MTGA and VSM techniques (according to the instruments manual). On the other hand, a careful calibration procedure for all equipments was performed with the proper standards in each case in order to preclude systematic errors.

3. Results

3.1. Microstructure

XRD diffractograms for all the alloy ribbons are shown in Fig. 1. Initial compositions present a single broad peak indicative of a fully glassy structure, as confirmed by TEM observations, which exhibits a single diffuse halo (see inset in Fig. 1 corresponding to x = 0.0). By contrast, for samples with x = 7.5 and x = 10.0, some additional peaks are observed at 2θ = 52.7° (x = 7.5) and at 2θ = 52.48° and 77.18° (x = 10.0) which were associated to the (110) and (220), (620) planes of the cubic Fe_3(Si, Ge) and the Fe_3Ge phases, respectively (according to the ICDD files 065-0994 and 03-065-9102). These diffraction peaks are indicative of a progressive crystallization process upon Ge substitution. For x = 10.0, an increased crystallized volume fraction is supported by the TEM micrographs displayed in Fig. 2, for which a composite structure comprising an amorphous phase together with small precipitates lower than 20 nm (Fig. 2a) is observed. The corresponding diffraction pattern (Fig. 2b) includes some few spots immersed into the diffuse haloes, related to additional crystallization of the residual amorphous phase present in the samples after the initial crystallization. They correspond to the (111), (200), (220), (222) and (400) diffraction planes of the Fe_3Ge phase. These crystalline inclusions are proof of the growth of the Fe3Ge crystalline phase from the amorphous matrix. The well-defined splitting on the diffraction rings indicates that the crystallites possess long-range order.

3.2. Crystallization kinetics and glass forming ability

Fig. 3 shows DSC curves for the $Fe_{80}B_{10}Si_{10-x}Ge_x$ alloy series, measured at a heating rate of 25 K/s. For Ge concentrations x < 10, all plots exhibit a two-step crystallization process, with two widely separated exothermic peaks. In each one there is an overlapped exothermic peak, it means that the first stage of crystallization occurred simultaneously in the samples with a primary crystallization peak T_{x1} between 716 K and 760 K, and a secondary crystallization peak T_{x2} above 800 K. The $Fe_{80}B_{10}Ge_{10}$ alloy sample exhibits no crystallization event, which is consistent with XRD and TEM results. For increasing Ge content, T_{x1} decreases, reflecting a reducing thermal stability upon

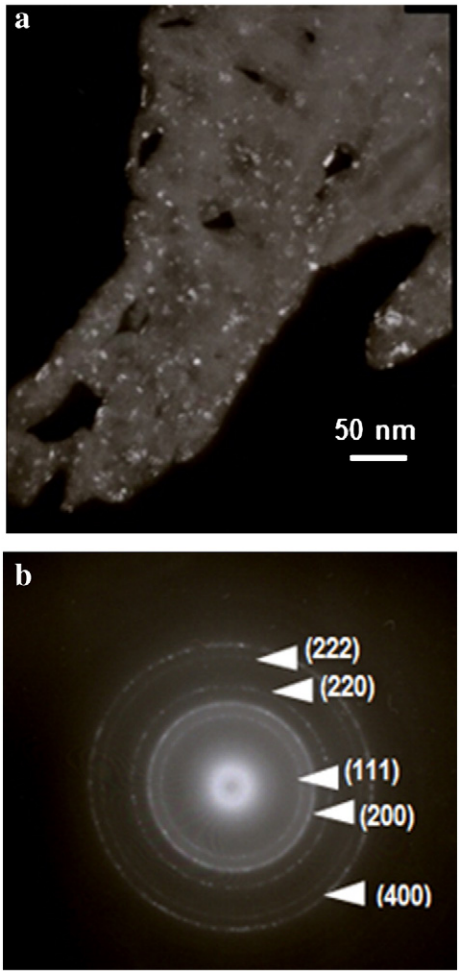

Fig. 2. TEM micrographs for the $Fe_{80}B_{10}Ge_{10}$ alloy: a) Dark field image exhibiting the nanocrystalline phase Fe_3Ge embedded in an amorphous matrix; b) the corresponding diffraction pattern (planes are indexed with the Fe_3Ge phase).

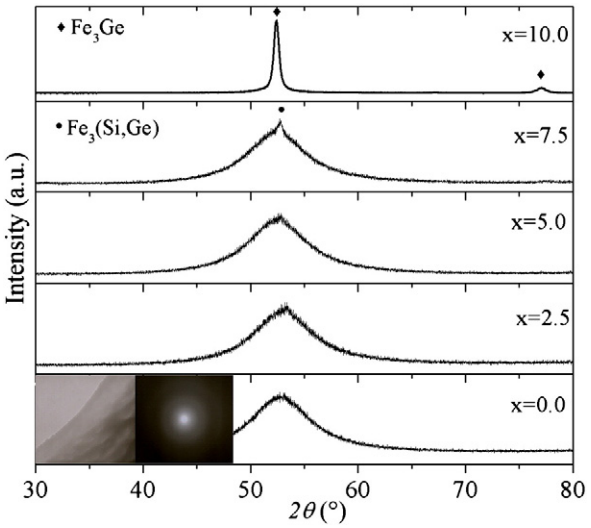

Fig. 1. XRD diffractograms and TEM micrographs for the $Fe_{80}B_{10}Si_{10-x}Ge_x$ alloy series. Inset: TEM micrograph and the corresponding selected area diffraction pattern for the $Fe_{80}B_{10}Si_{10}$ alloy sample.

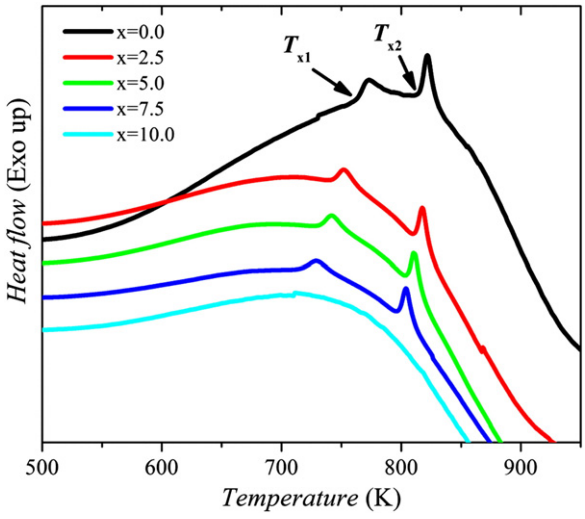

Fig. 3. DSC curves for the $Fe_{80}B_{10}Si_{10-x}Ge_x$ alloy series at a heating rate of 25 K/s. The two-step crystallization process of the amorphous phase is clearly manifested as exothermic reactions, for which the primary and secondary temperatures T_{x1} and T_{x2} indicate the onset of each event.

Ge substitution across the compositional series. The T_{x1} represents the upper limit of use for having an amorphous matrix as the main microstructure feature for present Ge-containing alloys. Additionally, the DSC curves of the alloys with x = 0.0 and x = 10.0 exhibit a small platform before the sharper peak. This could be attributed to the non-steady nucleation taking place very rapidly in the initial stages of the crystallization exotherm. It has been pointed out [33] that the crystallization exotherm characterizes the growth of the crystalline phase from the amorphous matrix and the nucleation is more or less calorimetrically unobservable at temperatures below the crystallization exotherm. In the case of the alloy with x = 10.0 the slight platform can be associated with any residual amorphous phase that crystallizes and is almost unobservable calorimetrically. A summary of crystallization temperatures is shown in Table 1.

On the other hand, Fig. 4 displays DSC curves for the $Fe_{80}B_{10}Si_{10}$ at different heating rates. From these data we determined the activation energy E for crystallization by means of the Kissinger model, via the following equation [34]:

$$\ln\left(\frac{T_p^2}{\beta}\right) = \frac{E}{RTp} + C$$

where β is the heating rate, R is the gas constant, T_p corresponds to the peak crystallization temperature and C is a constant. By plotting $\ln(T_p^2/\beta)$ vs T_p^{-1}, the resultant straight line indicates that the Kissinger model for crystallization can be applied for present Ge-containing amorphous alloys (Fig. 5). The energy E can be calculated for the remaining compositions in the same fashion (Table 1). The reducing tendency for E suggests a deleterious effect on the glass forming ability of the alloys with increasing Ge content, as supported by XRD results and TEM observations.

3.3. Magnetic properties

3.3.1. VSM measurements

The saturation magnetization M_s and coercivity H_c (determined from hysteresis loops measured by VMS technique) for the $Fe_{80}B_{10}Si_{10-x}Ge_x$ alloy series are shown in Fig. 6. Initially, M_s decreases with Ge content from 1.58 T to 1.50 T (for x = 0.0 and 2.5), followed by a recovery at x = 5.0. There is no obvious change of M_s for higher Ge contents. On the other side, H_c displays a progressive increment across the compositional series, reaching a maximum of 2.0 kA/m for x = 10.0. The values of M_s and H_c are shown in Table 2.

3.3.2. Curie temperature

The Curie temperature T_c of the amorphous phase across the compositional series $Fe_{80}B_{10}Si_{10-x}Ge_x$ exhibits an increasing tendency with Ge content, as it is illustrated in Fig. 7. For Ge concentrations lower than 7.5, a single step in the MTGA curve reflected the Curie transition of the amorphous phase (see inset Fig. 7). In contrast, for the x = 7.5 sample, the corresponding MTGA curve shown in Fig. 8a manifests a multi-step behavior, with three Curie points transitions, which can be ascribed to the amorphous phase (T_{c1}, around 700 K), the crystalline phase Fe_3Si (T_{c2}, near to 800 K [35]) and one last transition, T_{c3}, that can be related with another $Fe_3(Si,Ge)$ phase around 900 K, which was not found within the limits of sensitivity of the XRD technique. On the other hand, for the x = 10.0 sample (Fig. 8b), the transition T_{c4} observed near to 725 K can be attributed to the crystalline phase Fe_3Ge with T_c = 740 K [36]. Due to the lack of appreciable amorphous phase for this Ge-containing alloy, one last transition T_{c5} is observed at 925 K which can be associated with another Fe_3Ge phase. All Curie transitions are consistent with XRD and TEM data.

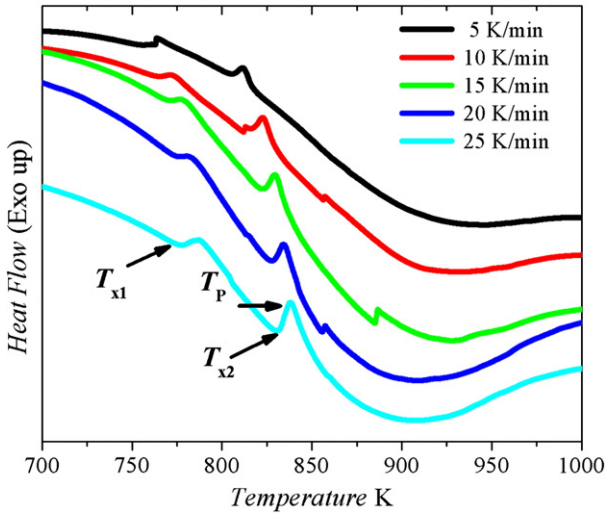

Fig. 4. DSC curves for the $Fe_{80}B_{10}Si_{10}$ alloy sample at a variable heating rate. The peak temperature T_p is indicated for activation energy calculations.

3.3.3. Ferromagnetic resonance (FMR)

The FMR spectra for the $Fe_{80}B_{10}Si_{10-x}Ge_x$ alloy series is shown in Fig. 9, for which the resonance field H_{res} can be determined as the field where dP/dH = 0 line cuts the dP/dH vs H curve. Up to Ge content of x = 7.5, the alloy samples exhibit a single FMR absorption near to 720 Oe, whereas for the x = 10.0 sample, two additional absorptions appear at a slightly lower and higher fields of 650 Oe and 750 Oe, respectively. The second resonant absorption can be attributed to a

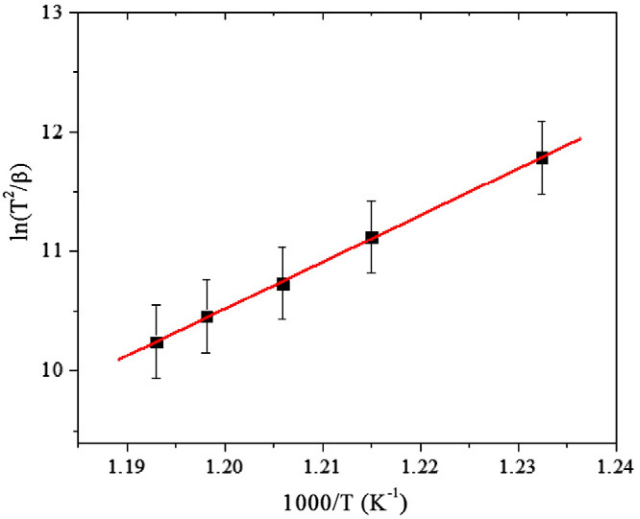

Fig. 5. Kissinger plot for the $Fe_{80}B_{10}Si_{10}$ amorphous alloy. The linear fitting is shown in red with a R^2 parameter of 0.998.

Table 1
Primary and secondary temperatures for crystallization peaks T_{x1}, T_{x2}, peak crystallization T_p and activation energy E, according to the Kissinger model, for the alloy samples $Fe_{80}B_{10}Si_{10-x}Ge_x$ (x = 0.0, 2.5, 5.0).

Ge content x	$T_{x1}(K)$ (25 K/min)	$T_{x2}(K)$ (25 K/min)	$T_P(K)$ (25 K/min)	E_C (kJ/mol)
0	775.89 ± 30	830.32 ± 10	840.46 ± 30	326.21 ± 19
2.5	756.61 ± 10	826.20 ± 20	833.34 ± 15	324.05 ± 60
5.0	745.65 ± 10	818.22 ± 15	825.72 ± 10	297.87 ± 30

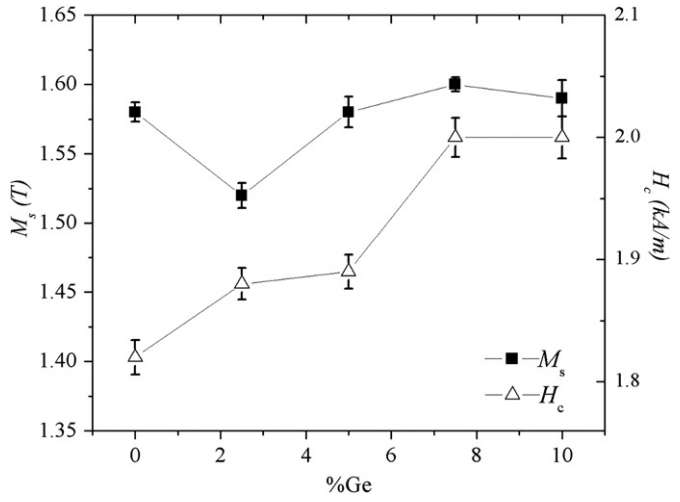

Fig. 6. Magnetic properties M_s and H_c as a function of Ge content for the $Fe_{80}B_{10}Si_{10-x}Ge_x$ alloy series (solid lines represent a guide for the eye, only).

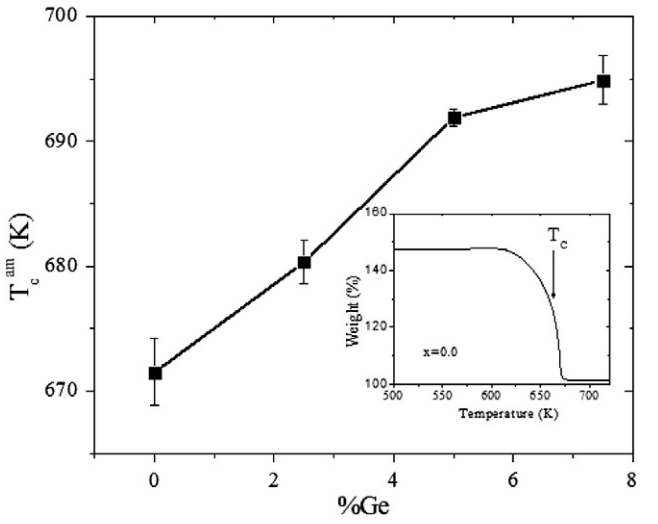

Fig. 7. Curie temperature as a function of Ge content for the $Fe_{80}B_{10}Si_{10-x}Ge_x$ alloy series (connecting line represents a guide for eye, only). The inset shows the Curie transition for the $Fe_{80}B_{10}Si_{10}$ sample.

secondary magnetic phase, namely the crystalline Fe_3Ge phase [37,38]. The trend of M_s with Ge concentration was checked by mean of FMR experiments. We can obtain the value of M_s from resonance conditions for an infinite film plane using the relation [39]:

$$\left(\frac{w}{y}\right)^2 = 4\pi M_z H_z + H_z^2$$

where $\omega = 2\pi f$ is the angular frequency, γ is the gyromagnetic ratio, $Mz = M_s$ and $Hz = H_{RES}$ (resonance field, defined as the field where the $dP/dH = 0$ line cuts the dP/dH versus H curve). M_s values obtained from the above equation are shown in Table 3.

4. Discussion

For Ge concentration values of up to $x = 5.0$, the alloys exhibited a fully glassy structure, as manifested by the XRD, TEM and MTGA results. For $x > 5.0$, the crystallization process is favored by the reducing activation energy E observed as the Ge content increases from $x = 0.0$ to 5.0, which implies that lower energy is required for crystal formation. Concerning magnetic properties, several models have been used to explain the magnetism in amorphous alloys, like coordination bonding and chemical ordering [40–42]. In this case, the reduction of the saturation magnetization observed for the 2.5 at.% Ge-containing alloy may be associated to a preliminary change of the local coordination of magnetic atoms (favoring for example, a more dense packed structure) affecting the magnetic moment per atom, as was pointed out by a previous work on the partial substitution of Ge for B in $Fe_{80}B_{20}$ amorphous alloys [43]. Further increase of Ge atoms (with larger atom radius compared with Si, for example, atom radius difference for the Ge–Si pair is of 7.5%, while for the Ge-B pair is of 51.2%, noticeably larger than the 40.6% of the Si–B pair [44]) contributes to the expansion of the amorphous structure, moving away Fe–Fe pairs, yielding to less densely packed structure and hence, affording the recovery of the magnetic moment observed for $x > 2.5$. Beyond $x = 5.0$, the precipitation of crystalline secondary magnetic phases contributes to the stabilization of the saturation magnetization values. This behavior of M_s with the Ge content is in good agreement with previous results reported for Finemet alloys containing Ge [29] and is supported by FMR results. The saturation magnetization deduced from FMR experiments (Table 3) is lower than the one obtained in the DC field experiments (Table 2). A possible explanation for this discrepancy comes from the same fact that explains the GMI (Giant Magneto-Impedance) effect: at high frequency, penetration depth of microwave field is smaller than the thickness of the metallic ribbon. Thus, only a certain surface layer of the ribbon is actually sensing to external AC field. In that case, the saturation magnetization is an "effective" magnetization (that of the material fraction actually affected by the external AC field) resulting in a lower value of M_s [45]. Additionally, the presence of crystallites for $x \geq 7.5$ provides numerous structural defects acting as pinning centers, which in turn determines the marked increase in H_c observed for such Ge concentrations (Fig. 5). The Curie temperature variation for the amorphous phase (Fig. 6) reflects the atomic redistribution processes caused by the incorporation of large Ge atoms, up to $x = 5.0$, and to the partial crystallization for $x = 7.5$, which implies a change of the number of nearest neighbors as well as of the interatomic Fe–Fe distances, which in turn leads to enhanced exchange integrals for the Fe–Fe interaction and hence, to the improved

Table 2
Saturation magnetization for the alloy samples $Fe_{80}B_{10}Si_{10-x}Ge_x$ ($x = 0.0$, 2.5, 5.0, 7.5, 10.0) obtained in DC field measurements.

Parameter	$x = 0$	$x = 2.5$	$x = 5.0$	$x = 7.5$	$x = 10.0$
M_s(T) (VSM)	1.58 ± 0.1	1.50 ± 0.2	1.58 ± 0.4	1.60 ± 0.1	1.59 ± 0.5

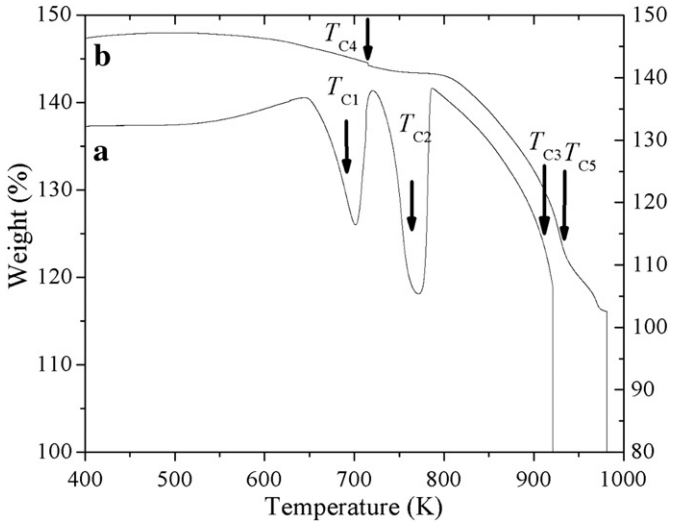

Fig. 8. MGTA curves corresponding to the $Fe_{80}B_{10}Si_{10-x}Ge_x$ alloys with $x = 7.5$ (a) and $x = 10.0$ (b). Distinctive Curie transitions can be associated to different magnetic phases.

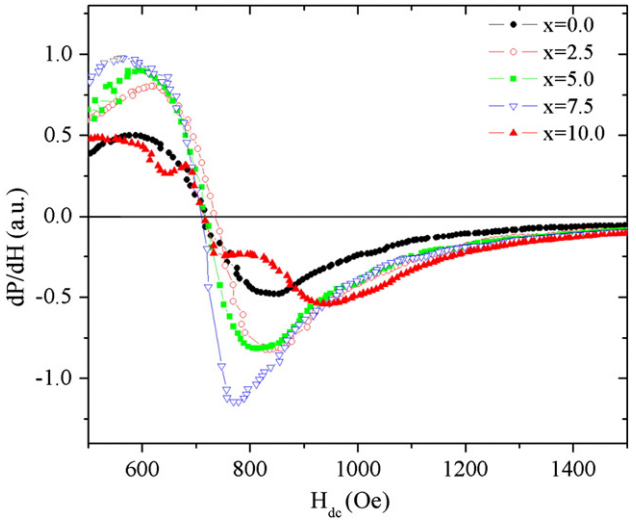

Fig. 9. FMR spectra for the amorphous alloys series $Fe_{80}B_{10}Si_{10-x}Ge_x$. The additional absorption signals for the sample with x = 10.0 are indicative of a secondary magnetic phase (crystalline Fe_3Ge).

Table 3
Resonance field and saturation magnetization for the alloy samples $Fe_{80}B_{10}Si_{10-x}Ge_x$ (x = 0.0, 2.5, 5.0, 7.5, 10.0) deduced from FMR experiments.

Parameter	x = 0	x = 2.5	x = 5.0	x = 7.5	x = 10.0
H_{RES} (Oe)	712.08 ± 30	744.67 ± 20	709.57 ± 10	699.54 ± 30	717.09 ± 40
$4\pi M_s$ (T)	1.52 ± 0.1	1.44 ± 0.4	1.53 ± 0.3	1.55 ± 0.1	1.51 ± 0.2

T_c tendency. This correlation has been described in similar FeB amorphous alloys [19]. In addition, from FMR measurements, it can be inferred that from the x = 7.5 sample, the resonant response of the nanocrystalline phase is coupled with the amorphous matrix, which results in a single magnetic response. In contrast, for the x = 10.0 alloy, a decoupling between the two resonant signals (amorphous and nanocrystals) is manifested.

5. Conclusions

The glass forming ability and microstructure of melt-spun $Fe_{80}B_{10}Si_{10-x}Ge_x$ alloys is strongly influenced by Ge content, which in turn had a deleterious effect on the alloys' glass forming ability, allowing the progressive crystallization of the amorphous phase in as-quenched alloys for x ≥ 7.5. On the other hand, the magnetic properties (M_s, H_c, T_c) also resulted highly sensitive to the microstructural evolution promoted by the increasing Ge concentration, yielding to a magnetic hardening as manifested by the coercivity of the alloys and the FMR measurements.

Acknowledgments

Authors are grateful with Carlos Flores and Esteban Fregoso (IIM-UNAM) by their valuable technical assistance.

References

[1] W. Klement, R.H. Willens, P. Duwez, Nature 187 (1960) 869.
[2] H.W. Kui, A.L. Greer, D. Turnbull, Appl. Phys. Lett. 45 (1984) 615.
[3] A. Peker, W.L. Johnson, Appl. Phys. Lett. 63 (1993) 2342.
[4] H. Gavrila, V. Ionita, J. Optoelectron. Adv. Mater. 4 (2002) 173.
[5] G. Krabbes, G. Fuchs, W.-R. Canders, H. May, R. Palka, High Temperature Superconductor Bulk Materials: Fundamentals–Processing–Properties Control–Application Aspects, Wiley-VCH, Germany, 2006 2006.
[6] S. Eskandarany, A. Inoue, Metall. Mater. Trans. A 37A (2006) 2231.
[7] Y.F. Sun, N. Tsuji, S. Kato, S. Ohsaki, K. Hono, Mater. Trans. 48 (2007) 1605.
[8] O. Ohsaki, S. Kato, N. Tsuji, T. Ohkubo, K. Hono, Acta Mater. 55 (2007) 2885.
[9] G.Y. Wang, P.K. Liaw, M.L. Morrison, Intermetallics 17 (2009) 579.
[10] C.H. Smith, in: H.H. Liebermann (Ed.), Rapidly Solidified Alloys, Marcel Dekker, New York, 1993, p. 617.
[11] G. Herzer, Amorphous and nanocrystalline materials, in: K.H.J. Buschow (Ed.), Concise Encyclopedia of Magnetic and Superconducting Materials, 2nd ed., Elsevier, Amsterdam, 2005, p. 16.
[12] P. Allia, M. Coisson, P. Tiberto, F. Vinai, Soft magnetic properties of rapidly solidified alloys, Magnetic Amorphous Alloys: Structural, Magnetic and Transport Properties, Research Signpost, Trivandum India, 2003, p. 23.
[13] R.C. O'Handley, Modern Magnetic Materials: Principles and Applications, John Wiley&Sons, New York, 2000.
[14] G. Tae Bae, S. Bok Lee, N.J. Kim, Mater. Sci. Eng., A 449 (2007) 489.
[15] P. Kwapuliński, Z. Stokłosa, J. Rasek, G. Badura, J. Magn. Magn. Mater. 320 (2008) 778.
[16] J.J. Ipus, J.S. Blázquez, V. Franco, A. Conde, J. Magn. Magn. Mater. 496 (2010) 7.
[17] Ch. Chang, B. Shen, A. Inoue, Appl. Phys. Lett. 89 (2006) 051912.
[18] Y. Sun, X. Bi, JALCOM, 2010, http://dx.doi.org/10.1016/j.jallcom.2010.09.107.
[19] M.L. Fdez-Gubieda, A. Garcia-Arribas, J.M. Barandiarán, R. López, Phys. Rev. B 62 (2000) 5746.
[20] A. Hirata, Y. Hirotsu, T. Ohkubo, T. Hanada, V.Z. Bengus, Phys. Rev. B 74 (2006) 214206.
[21] M. Aykol, A.O. Mekhrabov, M.V. Akdeniz, Acta Mater. 57 (2009) 171.
[22] C. Hausleitner, J. Hafner, Phys. Rev. B 47 (1993) 5689.
[23] Y.B. Xu, D. Greig, E.A. Seddon, J.A.D. Matthew, J. Appl. Phys. 87 (2000) 7136.
[24] J. Hafner, M. Tegze, C. Becker, Phys. Rev. B 49 (1994) 285.
[25] J.W. Taylor, J.A. Duffy, A.M. Bebb, M.J. Cooper, Phys. Rev. B 63 (2001).
[26] H. Tian, C. Zhang, J. Zhao, C. Dong, B. Wen, Q. Wang, Phys. Rev. B 407 (2012) 250.
[27] A. Inoue, J. Seon, Mater. Trans. 36 (1995) 1282.
[28] Y. Sun, X. Bi, J. Alloy Compd. 509 (2011) 1665.
[29] J.A. Moya, J. Magn. Magn. Mater. 322 (2010) 1784.
[30] D. Muracaa, V.J. Cremaschi, H. Sirkin, J. Magn. Magn. Mater. 311 (2007) 618.
[31] J.S. Blázquez, S. Roth, A. Conde, J. Alloy Compd. 395 (2005) 313.
[32] K. Suzuki, J.M. Cadogan, K. Aoki, S.P. Ringer, J. Magn. Magn. Mater. 254–255 (2003) 441.
[33] E. Illekova, J. Non-Cryst. Solids 68 (1984) 153.
[34] H.E. Kissinger, Anal. Chem. 29 (1957) 1702.
[35] M. Hong, J. Cryst. Growth 111 (1991) 984.
[36] J.W. Drijver, S.G. Sinnema, J. Phys. F 6 (1976) 11.
[37] D.S. Schmool, P. Gorria, J.M. Barandiarán, J. Appl. Phys. 81 (1997) 4048.
[38] H. Montiel, G. Alvarez, Physica B 384 (2006) 297.
[39] Kittel, Phys. Rev. 73 (1948) 2.
[40] R.C. O'Handley, J. Appl. Phys. 62 (1987) R15–R49.
[41] B. Yao, Y. Zhang, L. Si, H. Tan, Y. Li, J. Phys. Condens. Matter 16 (2004) 6325–6334.
[42] Daniel B. Miracle, Nature 3 (2004) 697.
[43] K.N. Soshow, T. Masumoto, M. Mitera, J. Magn. Magn. Mater. 15–18 (1980) 1331.
[44] O.N. Senkov, D.B. Miracle, Mater. Res. Bull. 36 (2001) 2183.
[45] M. Domínguez, J.M. García-Beneytez, M. Vázquez, S.E. Lofland, S.M. Bhagat, J. Magn. Magn. Mater. 249 (2002) 117.